Journal of Materials Chemistry A

PAPER

View Article Online
View Journal | View Issue

Cite this: J. Mater. Chem. A, 2019, 7, 14790

Excellent carrier transport materials produced by controlled molecular stacking and their application in flexible organic electronic devices†

Yong Woon Han, [a] Ho Jun Song, [b] Sung Jae Jeon, [a] Hyoung Seok Lee,[a] Eui Jin Ko, [a] Chang Eun Song, [cd] Tae Hyun Sung [e] and Doo Kyung Moon *[a]

Research studies based on flexible organic electronic devices regarding the relationship between carrier transport and molecular stacking are actively reported. For enhancing carrier transport and mechanical strength, new types of anthracene derivatives (**ANT**), exhibiting parallel dominant molecular stacking characteristics, are designed and synthesized. They show parallel dominant molecular stacking properties inducing excellent carrier transport through hybridization with perpendicular materials. They are introduced as electron transport layers (ETLs) for organic solar cells (OSCs), organic light emitting diodes (OLEDs), and organic nano-generators (ONGs). Hybrid ETLs show excellent carrier transport characteristics, exhibiting minimized energy loss and suppressed carrier recombination resulting from relative resonance through partial polarization of **ANT**. Consequently, the power conversion efficiency (PCE) of the fabricated OSCs based on fullerene and non-fullerene systems reaches 9.6% and 11.4%, and the luminescence of OLEDs reaches up to 17 057 cd m^{-2}. In addition, flexible OSCs, OLEDs, and ONGs show improved output performance and mechanical strength due to excellent carrier transport. Especially, in flexible ONGs, high carrier transport can be helpful for enhancing output voltage by energy level shifting.

Received 27th February 2019
Accepted 21st May 2019

DOI: 10.1039/c9ta02213a

rsc.li/materials-a

Introduction

Organic optoelectronic devices (OOEDs) have been applied in various fields due to the advantages of organic semiconductors including low cost, flexibility, solution fabrication method, *etc.*[1–3] In particular, organic solar cells (OSCs) that convert light into electric power and organic light emitting diodes (OLEDs) that convert electric power into light are the representative OOEDs. OSCs and OLEDs consist of a multi-layered structure, including a buffer layer and photoactive layer, introduced in between the electrodes. Furthermore, OSCs and OLEDs have the advantages of being capable of accomplishing high performance through modification of the molecular design and device structure, *etc.*[4–12]

Regarding the high efficiency and stability of OOEDs, carrier transport is particularly important for OSCs and OLEDs, and it has opposite functions in respective similar structures. In OSCs, excitons are formed through light absorbed into a photoactive layer with a bulk-heterojunction (BHJ) structure, consisting of an organic donor and acceptor. Thereafter, photovoltaic characteristics appear through the charge dissociation and transport process. Then, the performance of OSCs is triggered by the carrier transport properties of photo-generated carriers. From this point of view, carrier transport properties can be greatly influenced by trap-assisted recombination or bimolecular recombination, resulting in low carrier mobility, which is affected by the inherent limitation of organic semiconductors.[4–6,13–16] By contrast, the mechanism of carrier recombination is essential for enhancing the performance of OLEDs.[17,18] However, there are some problems, such as non-radiative trap-assisted recombination during carrier transport, that need to be resolved.[17,19,20] Thus, the enhancement of carrier transport properties is mandatory for high performance of OSCs and OLEDs.

Currently, studies are actively being performed with a focus on enhancing the carrier transport properties of OSCs and OLEDs. The first strategy, developed for enhancing carrier transport

[a]Nano and Information Materials Lab. (NIMs Lab.), Department of Chemical Engineering, Konkuk University, 120 Neungdong-ro, Gwangjin-gu, Seoul 05029, Republic of Korea. E-mail: dkmoon@konkuk.ac.kr; Fax: +82-2-444-0765; Tel: +82-2-450-3498

[b]Research Institute of Sustainable Manufacturing System Intelligent Sustainable Materials R&D Group, Korea Institute of Industrial Technology, 89 Yangdaegiro-gil, Ipjang-myeon, Seobuk-gu, Cheonan-si, Chungcheongnam-do, 331-822, Republic of Korea

[c]Energy Materials Research Center, Korea Research Institute of Chemical Technology (KRICT), 141 Gajeongro, Yuseong, Daejeon 34114, Republic of Korea

[d]Advanced Materials and Chemical Engineering, University of Science and Technology (UST), 217 Gajeongro, Yuseong, Daejeon 34113, Republic of Korea

[e]Department of Electrical Engineering, Hanyang University, Wangsimni-ro, Seongdong-gu, Seoul 04763, Republic of Korea

† Electronic supplementary information (ESI) available. See DOI: 10.1039/c9ta02213a

properties, involves changes in the molecular design and composition of the photoactive layer.[21,22] Chen and co-workers developed a low-bandgap non-fullerene acceptor by fine-tuning the energy level, and reported a power conversion efficiency (PCE) of 12.21% due to improvements in the photocurrent properties of OSCs fabricated with PBDB-T (poly[(2,6-(4,8-bis(5-(2-ethylhexyl) thiophen-2-yl)-benzo[1,2-*b*:4,5-*b*′]dithiophene))-*alt*-(5,5-(1′,3′-di-2-thienyl-5′,7′-bis(2-ethylhexyl)benzo[1′,2′-*c*:4′,5′-*c*′]dithiophene-4,8-dione))]).[21] In addition, Wang and co-workers reported a PCE of 9.25% due to an increase in photocurrent in OSCs fabricated with $PC_{71}BM$ ([6,6]-phenyl C_{71}-butyric acid methyl ester), the fullerene acceptor, and ITIC (3,9-bis(2-methylene-(3-(1,1-dicyanomethylene)-indanone))-5,5,11,11-tetrakis(4-hexylphenyl)-dithieno[2,3-:2′,3′-*d*″]-*s*-indaceno[1,2-*b*:5,6-*b*′]dithiophene), the non-fullerene acceptor, in the photoactive layer based on PTZ1, the wide-bandgap donor.[22] These results have been commonly seen in studies aiming for the maximization of photo-generated carriers in the photoactive layer of OSCs.

The second strategy developed for enhancing carrier transport properties involves introducing a buffer layer with properties of high mobility.[23–31] Chen and co-workers fabricated OSCs through the introduction of conjugated-polyelectrolytes (CPEs), which were developed to replace PEDOT:PSS (poly(3,4-ethylenedioxythiophene):polystyrene sulfonate) as the hole transport layers (HTLs). These OSCs based on PTB7-Th (poly[4,8-bis(5-(2-ethylhexyl)thiophen-2-yl)benzo[1,2-*b*;4,5-*b*′]dithiophene-2,6-diyl-*alt*-(4-(2-ethylhexyl)-3-fluorothieno[3,4-*b*]thiophene-)-2-carboxylate-2-6-diyl]) and $PC_{71}BM$ exhibited a PCE of 9.6%.[23] Our group also succeeded in fabricating high-performance and high-stability OSCs with a PCE of 8.3% based on PTB7-Th:$PC_{71}BM$ through the development and introduction of neutral CPEs as the HTLs.[24] Furthermore, Hou and co-workers developed electron transport layers (ETLs) based on naphthalene diimide (NDI) units possessing high crystallinity, and reported a PCE of 13.9% by enhancing carrier transport properties.[25] In addition, Lu and co-workers fabricated polymer light emitting diodes (PLEDs) with inorganic HTLs of CuSCN and CuI, and reported improved luminous efficiency (16.8 cd A^{-1}) owing to excellent hole collection properties.[26] Yang, He, and co-workers fabricated PLEDs in which PEIE (polyethyleneimine ethoxylate) and TPBI (1,3,5-tris(*N*-phenylbenzimidazol-2-yl)benzene) were introduced as ETLs, and reported an improvement in the luminous efficiency (6.8 cd A^{-1}) as a result of increased electron collection.[27]

In particular, there are buffer materials such as PEDOT:PSS, used as HTLs, and **PFN** (poly[(9,9-bis(3′-(*N*,*N*-dimethylamino) propyl)-2,7-fluorene)-*alt*-2,7-(9,9-dioctylfluorene)]), used as ETLs, which are the representative buffer layers used for OSCs and OLEDs. However, the disadvantages include a reduction in device stability due to the acidic characteristics of PEDOT:PSS,[32–34] and the dependence of thickness (~10 nm) due to the low carrier mobility characteristics of organic buffer layers such as **PFN**, *etc.*[35,36] Therefore, the demand for studies investigating new buffer layers that can overcome such disadvantages is increasing continuously.

The third strategy developed with an aim to improve carrier transport properties involves introducing the hybrid buffer layer with enhanced carrier mobility. The introduction of a hybrid buffer layer with inorganic semiconductors can be shown to lead to a high carrier mobility in order to compensate for the low carrier transport properties of organic semiconductors.[37–39] In addition, forming the hybrid active layer, which the buffer materials with self-assembled alignment properties were enabling, enhanced the carrier transport properties and simplified the fabrication process.[40,41]

In the present study, the anthracene derivative (namely **ANT**) materials were synthesized with a focus on improving carrier transport properties; then the OSCs and OLEDs were fabricated by introducing ETLs. Anthracene derivatives are frequently used as an emissive layer of OLEDs, due to their excellent electrochemical characteristics, high mobility, and high color purity.[42–45] Since the formation of the π–π stacked structure of the anthracene core is enabled, they are expected to exhibit excellent carrier transport properties.[45,46]

In contrast to **PFN**, the commercial ETLs which exhibited perpendicular random orientation, **ANT** exhibited parallel dominant molecular stacking characteristics due to the anthracene core and formed an array that was advantageous for carrier transport. **ANT** exhibited parallel dominant molecular stacking characteristics due to the anthracene core and formed an array that was advantageous for carrier transport. As a result, the improvements in J_{SC} and FF were higher than those for **PFN**, with approximately 9.4% maximal PCE in the fullerene-based system OSCs with enhanced carrier transport properties. Furthermore, the 9.6% maximal PCE was due to the formation of hybrid ETLs of **ANT** and **PFN** with maximized carrier transport properties. Such an enhancement of performance was also applied to the non-fullerene-based system where a high PCE of 11.4% was achieved. Similarly, the OLEDs fabricated through the introduction of hybrid ETLs of **ANT** and **PFN** exhibited high performance with a maximum luminescence of 17 057 cd m^{-2}.

Furthermore, hybrid ETLs were also applied to flexible OSCs, OLEDs, and organic nano-generators (ONGs), exhibiting enhanced mechanical strength and output performances. The hybrid ETLs exhibited well-maintained performance in flexible OSCs and OLEDs during mechanical bending tests. Especially, the hybrid ETLs in the fabricated ONGs exhibited large enhancement of charging voltage characteristics under irradiation conditions. These results indicate that the high carrier transport properties and mechanical strength of hybrid ETLs can be applied not only in the field of flexible organic optoelectronics but also in flexible organic nano-generators.

Experimental section

Materials and methods

ANT introduced as ETLs was synthesized by following methods. Unless otherwise specified, all reactions were carried out under a nitrogen atmosphere. Solvents were dried by standard procedures. All column chromatographies were performed with the use of silica gel (230–400 mesh, Merck) as the stationary phase. ^{1}H NMR spectra were recorded with a Bruker ARX 400

spectrometer using $CDCl_3$ as the solvent and TMS as the internal standard.

Synthesis of monomers

2-Bromo-6-(6-bromohexyloxy)naphthalene (M1). 6-Bromo-2-naphthol (10 g, 44.82 mmol), 1,6-dibromobutane (43.7 g, 179.2 mmol), and potassium carbonate (24.7 g, 179.2 mmol) were dissolved in acetone (130 mL) and the mixture was refluxed for 24 hours under nitrogen. The solvent of the reaction mixture was removed under reduced pressure. After washing with water, ethanol was added to remove excess 1,6-dibromobutane, after which it was filtered. The precipitate was purified by silica gel column chromatography using $CHCl_3$ as the eluent. Yield 7.7 g (45%) (Scheme 1). ^{1}H NMR (400 MHz, $CDCl_3$, Me_4Si): $\delta = 7.88$ (s, 1H), 7.60 (d, 1H), 7.54 (d, 1H), 7.46 (d, 1H), 7.14 (d, 1H), 7.04 (d, 1H), 4.02 (t, 2H), 3.41 (t, 2H), 1.89 (m, 4H), 1.52 (m, 4H).

9,10-Bis(6-(6-bromohexyloxy)naphthalene-2-yl)anthracene (M2). To 2-bromo-6-(6-bromohexyloxy)naphthalene (2 g, 5.17 mmol) dissolved in THF (30 mL), 2.1 mL of *n*-butyllithium (2.5 M in hexane) was added slowly at −78 °C. To the suspension, 2-ethylanthraquinone (0.55 g, 2.35 mmol) in THF (20 mL) was added dropwise at −78 °C. The mixture was left to reach room temperature. Cold water (200 mL) was added and the organic phase separated. The water phase was extracted with ether (300 mL). The combined organic fractions were dried over sodium sulfate and the solvent was removed at a reduced pressure. To this residue were added potassium iodide (1.17 g, 7.05 mmol), sodium hypophosphite hydrate (2.06 g, 23.50 mmol), and acetic acid (30 mL), and the mixture was heated under reflux for 16 h. After cooling, the product was washed with plenty of water, and dried. The compound was purified by column chromatography over silica gel. Yield 1.57 g (85%) (Scheme 1). ^{1}H NMR (400 MHz, $CDCl_3$, Me_4Si): $\delta = 7.94$ (m, 3H), 7.82 (m, 2H), 7.69 (m, 4H), 7.56 (d, 2H), 7.50 (s, 1H), 7.28 (m, 5H), 7.20 (d, 1H), 7.10 (m, 1H), 4.18 (m, 4H), 3.23 (m, 4H), 1.89 (m, 12H), 1.30 (m, 3H), 1.15 (t, 3H), 0.86 (m, 3H).

2,2′,2″,2‴-((((Anthracene-9,10-diylbis(naphthalene-6,2-diyl))bis(oxy))bis(hexane-6,1-diyl))bis(azanetriyl))tetrakis(ethan-1-ol) (ANT). 9,10-Bis(6-(6-bromohexyloxy)naphthalene-2-yl)anthracene (0.1 g, 0.12 mmol) was dissolved in THF, and then diethanolamine (DEA, 0.5 g, 4.75 mmol) was added to the stirred mixture. The mixture was reacted at RT for 48 h and the solvent of the reaction mixture was removed under reduced pressure. The crude product was purified by recrystallization. Yield: 0.08 g (87%) (Scheme 1). ^{1}H NMR (400 MHz, $CDCl_3$, Me_4Si): $\delta = 7.87$ (m, 3H), 7.75 (m, 2H), 7.63 (m, 4H), 7.50 (d, 2H), 7.42 (s, 1H), 7.21 (m, 5H), 7.12 (d, 1H), 7.03 (m, 1H), 4.11 (m, 4H), 3.59 (m, 4H), 3.17 (m, 2H), 2.62 (m, 10H), 2.05 (m, 3H), 1.78 (m, 10H), 1.51 (m, 12H), 1.08 (t, 3H), 0.81 (m, 2H).

Materials and fabrication of OSCs

PTB7-Th (as a donor) and $PC_{71}BM$ (as an acceptor) used as the photoactive layer of the fullerene based OSCs were purchased from 1-Materials (Canada). PBDB-T (as a donor) and ITIC-M (as an acceptor of the non-fullerene system) were purchased from Brilliant Matters (Canada). Chlorobenzene (CB) and 1,8-diiodooctane (DIO) used as solvent and additives were purchased from Sigma-Aldrich (Germany). PEDOT:PSS (AI 4083) used as HTLs was purchased from Heraeus (Germany). **PFN** (PFN-P1) used as ETLs was purchased from 1-Materials (Canada). ITO glass (sheet resistance of 10 Ω sq^{-1}) used as an electrode for OSCs and OLEDs was purchased from AMG (Republic of Korea). Patterned ITO glass was cleaned *via* the ultra-sonication process with Alconox (neutral detergent), isopropyl alcohol (IPA), and deionized water (D.I. water) in this order. The cleaned ITO glass was subjected to UVO (UV–ozone) cleaning for 15 min in a UVO cleaner (Ahtech LTS AH 1700).

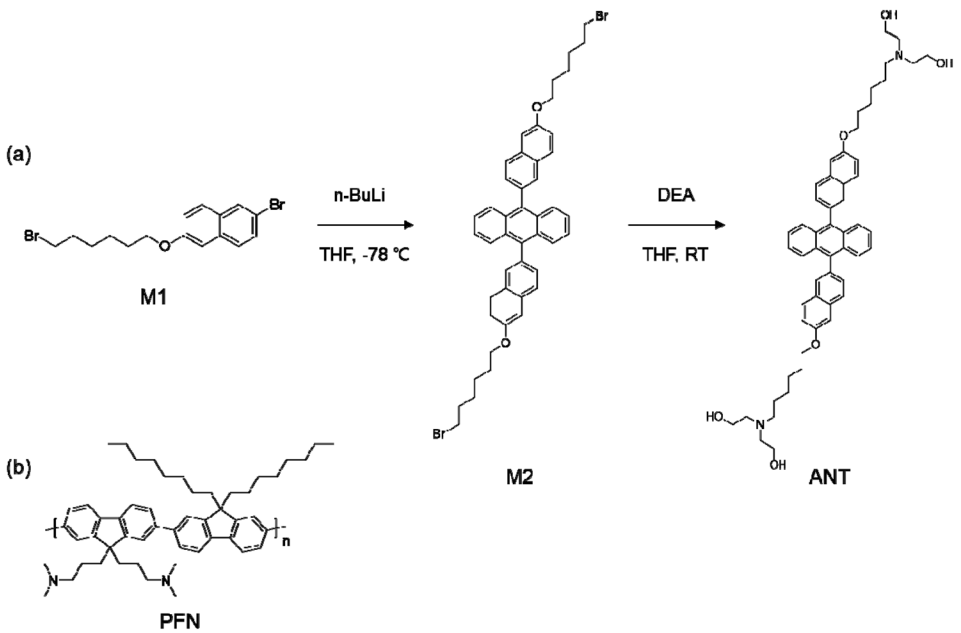

Scheme 1 (a) Schematic synthesis method of ANT and (b) structure of PFN.

The devices were fabricated with a conventional structure (ITO/PEDOT:PSS/BHJ layer/ETLs/Al). For HTLs, the PEDOT:PSS layer was formed onto UVO-cleaned ITO glass *via* the spin-coating method at 4000 rpm for 30 s, followed by thermal annealing at 140 °C for 10 min. A fullerene based BHJ layer was formulated with PTB7-Th and $PC_{71}BM$ (in a ratio of 1 : 1.5, 25 mg mL^{-1}) in CB (DIO 3 v/v%) solution, and then the BHJ layer was formed onto HTLs *via* the spin-coating method. A non-fullerene based BHJ layer was formulated with PBDB-T and ITIC-M (in a ratio of 1 : 1, 20 mg mL^{-1}) in CB (DIO 1 v/v%) solution, and then the BHJ layer was formed in the same way as for the fullerene system. For ETLs, **PFN** solution was formulated in methanol (2 mg mL^{-1}, acetic acid 4 μL). **ANT** solution was formulated in methanol (2 mg mL^{-1}, without acetic acid). The hybrid ETLs (**ANT** + **PFN**) were manufactured in various ratios (1 : 0, 8 : 2, 6 : 4, 1 : 1, 4 : 6, 2 : 8 and 0 : 1), and mixed in vials overnight. Each ETL was formed onto the BHJ layer *via* the spin coating method and dried for some time. After that, the metal electrode (Al) was thermally evaporated in a high vacuum chamber (at 1×10^{-7} Torr) with rates of 5.0 Å s^{-1}. Fabrication of flexible OSCs was performed in a similar manner with rigid OSCs on polyethylene-naphthalate (PEN)/ITO film.

Materials and fabrication of OLEDs

The green polymer comprising the photoactive layer of OLEDs was purchased from Sigma-Aldrich (Germany). In the same manner as for OSCs, PEDOT:PSS was formed onto cleaned ITO glass. The photoactive layer was formulated with the green polymer (10 mg mL^{-1}) in CB and film (*ca.* 100 nm) formed onto HTLs *via* the spin-coating method. The ETL solution was prepared by the same process as for OSCs. ETLs were formed onto the photoactive layer *via* the spin-coating method and dried for some time. After that process, the metal electrode (Al) was thermally evaporated in a high vacuum chamber (at 1×10^{-7} Torr) with rates of 5.0 Å s^{-1}. Fabrication of flexible PLEDs was performed in a similar manner to that of rigid PLEDs on PEN/ITO film.

Characterization of devices

The characterization of the current density–voltage (*J*–*V*), current density–light intensity and voltage–light intensity properties of the fabricated OSCs was performed with a Keithley 2400 source meter and solar simulator (Oriel, 1.5G AM under illumination of 100 mW cm^{-2}). The EQE was characterized with an incident power conversion efficiency (IPCE) measurement system (Mc Science, Polaronix K3100). UPS analysis was performed with an AXIS-NOVA (Kratos). XPS surface and depth profiling analyses were performed with a ULVAC-PHI 5000 VersaProbe (ULVAC). FE-SEM analysis was performed with an SU8010 (Hitachi). AFM analysis was performed with a PSIA XE-100 (Park Systems). The bending test of the flexible devices was performed with a bending tester (IV-solutions). The output voltage was measured with a DMM7510 graphical sampling multimeter (Keithley).

Results and discussion

In Scheme 1, the synthesis method of anthracene-based derivatives (namely **ANT**, Scheme 1a) and the structure of **PFN** (Scheme 1b) are exhibited. The **ANT**, the final compound, was purified several times by the re-crystallization process using methanol/H_2O, with a final yield of 87%, and the chemical structure was confirmed by ^1H NMR analysis (shown in Fig. S1–S3, ESI†). **ANT** exhibited higher solubility to polar solvents (such as methanol, ethanol, *etc.*).

The absorption characteristics and cyclic voltammetry characteristics of **ANT** are shown in Fig. S4 (ESI†). The maximum absorption peak of the **ANT** film appeared at 381 and 400 nm, while the absorption onset peak appeared at 435 nm (Fig. S4a, ESI†); the oxidation peak appeared at 1.03 V (Fig. S4b, ESI†). The calculated optical bandgap (E_g) was 2.85 eV; the levels of the highest occupied molecular orbital (HOMO) and the lowest unoccupied molecular orbital (LUMO) were $E_{HOMO} = -5.60$ eV and $E_{LUMO} = -2.75$ eV, respectively.

Fig. 1 shows the calculated electrostatic potential (ESP) images of **PFN** and **ANT**. The structures of **PFN** and **ANT** were calculated as optimized conformations in the ESP characteristics, respectively; two images of the front view and side view are presented. The scale bar includes negative potential (red color, high electron density) and positive potential (blue color, low electron density).[47,48] **PFN** (Fig. 1a) exhibited positive potential on the side chain and negative potential on the backbone. **ANT** (Fig. 1b) exhibited positive potential on the side chain and negative potential on the anthracene core and naphthalene unit. In particular, both molecules exhibited strong dipole moments (μ) to N atoms; the calculated dipole moments were $\mu_{PFN} = 0.6297$ D (Debye) and $\mu_{ANT} = 5.9335$ D, respectively. **PFN** showed a weak dipole towards the direction of N atoms from the main backbone. However, **ANT** exhibited strong dipole in the perpendicular direction at the anthracene core with strong

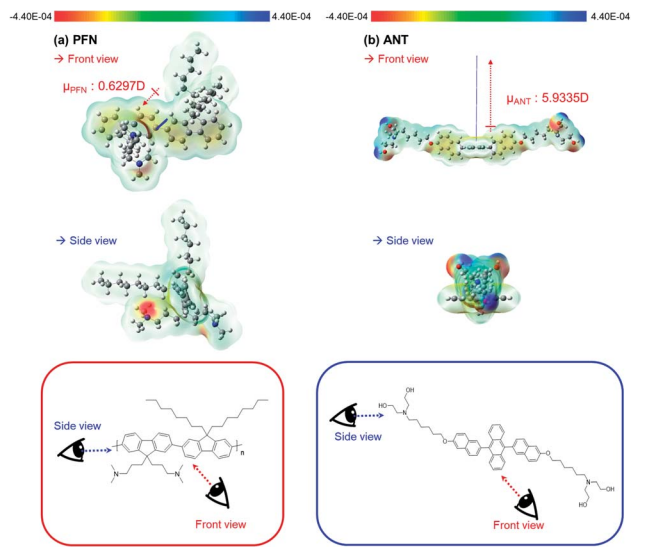

Fig. 1 Calculated ESP characteristics of (a) **PFN** and (b) **ANT** with respect to front view and side view.

negatively charged N atoms at the side groups. As a result, **ANT** exhibited strong attraction at the side groups through ESP calculation; therefore, excellent molecular stacking and carrier transport properties were predicted. Furthermore, the improved carrier transport path can be presumed to have resulted from hybridization of **ANT** and **PFN**, through the interaction between the highly electron rich amino group of **PFN** and the highly electron deficient diethanolamine group of **ANT**.

We performed GIWAXS analysis to confirm the molecular stacking characteristics of **PFN**, **ANT**, and the hybrid film (**ANT** + **PFN**) (referred to as the hybrid film below); the obtained 2D images are shown in Fig. 2 and the line-cut images of the out-of-plane and in-plane patterns are shown in Fig. S5 (ESI†). The **PFN** film exhibited a ring-like peak due to the existence of a random crystalline structure.[49,50] Also, **PFN** exhibited weak (001) and (001′) peaks at $q_{xy} = 0.4$ and 0.8 Å^{-1} with an azimuth angle of $0 \leq \Phi \leq 45$ due to a predominantly perpendicular random orientation against the substrate.[50–53] In contrast, the **ANT** film exhibited a strong (010) peak at $q_z = 1.74$ Å^{-1} ($d_{\pi-\pi} = 0.55$ nm), and (001) and (001′) ring-like peaks at $q_{xy} = 0.4$ and 0.8 Å^{-1} with an azimuth angle of $45 \leq \Phi \leq 90$ due to a predominantly parallel orientation against the substrate.[51] The hybrid film exhibited both a (010) peak at $q_z = 1.79$ Å^{-1} and a ring-like peak due to the parallel dominant random orientation.

In the solution state, they exhibited absorption in the $\lambda =$ 300–430 nm region (Fig. S6, ESI†). After film formation, the absorption characteristics were red-shifted slightly due to molecular ordering. Especially, the **ANT** and hybrid film exhibited a shoulder peak at $\lambda = 400$ nm. This result means that **ANT** and hybrid molecules formed ordered molecular stacking during film formation.[54] From the transmittance characteristics and contact angle with surface energy characteristics shown in Fig. S7 (ESI†), it can be seen that all films exhibited nearly 100% of transmittance characteristics after $\lambda = 430$ nm. Especially, the **ANT** and hybrid film exhibited over 80% transmittance characteristics in the $\lambda =$ 300–400 nm region. Also, the **ANT** (91.5°, 18.3°, and 25.91 mN m^{-1}) and hybrid film (86°, 27.0°, and 26.23 mN m^{-1}) exhibited lower surface energy characteristics calculated from contact angle measurement with water and chlorobenzene compared to **PFN** (77.1°, 33.1°, and 28.76 mN m^{-1}). Consequently, **PFN** formed the perpendicular dominant random orientation, while the **ANT** and hybrid film formed the parallel dominant molecular stacked order against the substrate. Through these analyses, we identified the molecular stacking characteristics calculated from ESP analysis based on a cubic unit and the results are illustrated in Fig. 2d. Furthermore, the ordered molecular stacking, high transmittance, and low surface energy characteristics of the **ANT** and hybrid film make them suitable as ETLs. These properties can be helpful for forming good interfacial matching and inducing high carrier transport properties when they are introduced as ETLs.

Fig. 3 and Table 1 show the structures of materials introduced into the BHJ layer and the structures of devices fabricated in this study, the current density–voltage (J–V) characteristics with deviation values and external quantum efficiency characteristics of the fabricated devices. The devices were fabricated with a conventional structure (ITO/PEDOT:PSS/BHJ layer/ETLs/Al), which introduced the BHJ layer based on PTB7-Th (as a donor, Fig. 3a) and $PC_{71}BM$ (as an acceptor, Fig. 3b). The structures of devices with the **PFN**, **ANT**, and hybrid film introduced as ETLs are presented in Fig. 3c. The device with **PFN** exhibited interfacial mixing, while the device with **ANT** and hybrid ETLs exhibited good contact interfacial properties (these are discussed in a later section).

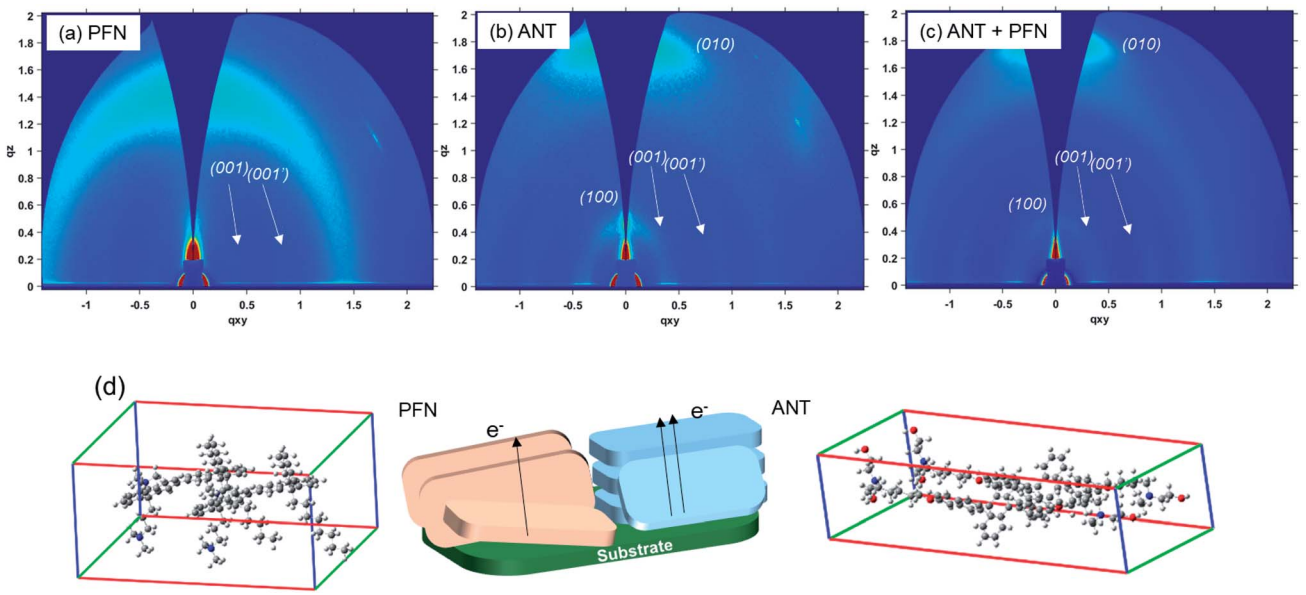

Fig. 2 GIWAXS characteristics of (a) **PFN**, (b) **ANT**, (c) the hybrid film (**ANT** + **PFN**), and (d) schematic image of molecular stacking characteristics of the cast films.

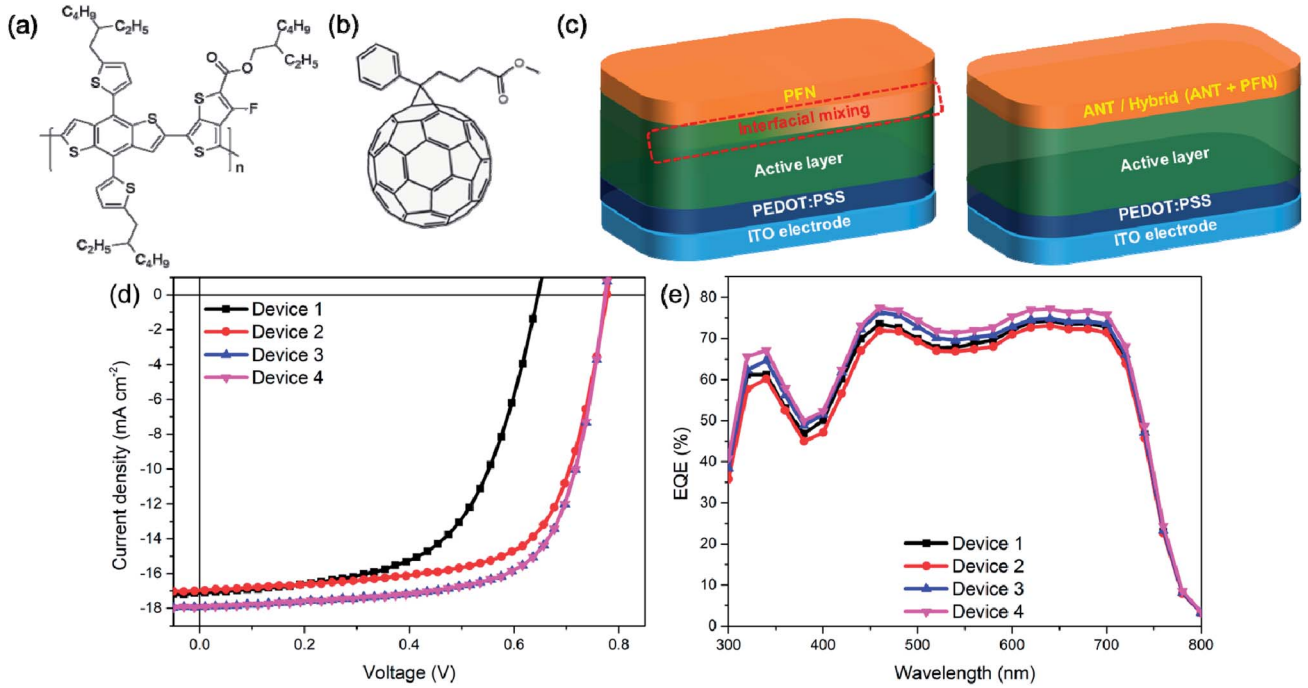

Fig. 3 Structures of (a) PTB7-Th as donors, (b) $PC_{71}BM$ as acceptors and (c) structures of the fabricated devices with each ETL, (d) current density–voltage (*J*–*V*) characteristics and (e) external quantum efficiency characteristics of the fabricated devices.

Device 1 was fabricated with a pristine BHJ, into which the ETLs had not been introduced; it exhibited a PCE of 6.5% (J_{SC} = 17.1 mA cm^{-2}, V_{OC} = 0.636 V, and FF = 60.0%). Into devices 2 and 3 were introduced each of **PFN** and **ANT** as ETLs, and they exhibited PCEs of 8.9% (J_{SC} = 17.0 mA cm^{-2}, V_{OC} = 0.777 V, and FF = 67.3%) and 9.4% (J_{SC} = 17.6 mA cm^{-2}, V_{OC} = 0.777 V, and FF = 68.7%), respectively. Device 4 was fabricated with **ANT** + **PFN** hybrid ETLs (referred to as hybrid ETLs below) and it exhibited the best PCE of 9.6% (J_{SC} = 17.9 mA cm^{-2}, V_{OC} = 0.777 V, and FF = 68.8%) (performance data optimized correspondingly to each ratio presented in Table S1, ESI†). V_{OC} (from 0.636 V to 0.777 V) and FF (from 60.0% to 67.3%) were improved by the introduction of **PFN**. However, J_{SC} (from 17.1 mA cm^{-2} to 17.6 mA cm^{-2}), V_{OC} (from 0.636 V to 0.777 V), and FF (from 60.0% to 68.7%) were greatly enhanced by the introduction of **ANT** with a higher PCE of 9.4%. Furthermore, the introduction of hybrid ETLs further improved both J_{SC} and FF, which resulted in the high PCE of 9.6%.

In the present study, the reasons behind the enhancement of device performance realized through the introduction of **ANT** and hybrid ETLs were interpreted in three ways. First, the perspective of change of energy barrier between the BHJ layer and cathode was interpreted with respect to the introduction of ETLs. Second, the performance enhancement was analyzed from the perspective of change of carrier recombination by the introduction of ETLs. Third, the viewpoint of carrier recombination and carrier transport mechanism was interpreted through identifying the morphology of the BHJ layer with incorporated ETLs.

In Fig. 4, the electronic characteristics of both the Al electrode (as a cathode) and the BHJ layer, into which ETLs were introduced, are presented through UPS analysis. Then, the relative energy levels resulting from the introduction of ETLs were compared to each other. Respective energy levels were calculated through the cut-off point and onset point of energy levels of binding energy, as expressed in the following equation.[45,55,56]

$$E = h\nu - (E_{\text{cut-off}} - E_{\text{onset}}) \quad (1)$$

Table 1 Photovoltaic performances of the fabricated OSCs (PTB7-Th:$PC_{71}BM$) with respect to ETLs[a]

Device structure	J_{SC} [mA cm^{-2}]	V_{OC} [V]	FF [%]	PCE[b] [%]
Device 1 (BHJ)	17.0 ± 0.11	0.616 ± 0.02	59.8 ± 0.21	6.5 (6.3 ± 0.12)
Device 2 (BHJ/**PFN**)	16.6 ± 0.40	0.767 ± 0.01	66.7 ± 0.61	8.9 (8.5 ± 0.20)
Device 3 (BHJ/**ANT**)	17.5 ± 0.10	0.767 ± 0.01	68.5 ± 0.16	9.4 (9.3 ± 0.10)
Device 4 (BHJ/**ANT** + **PFN**)	17.8 ± 0.11	0.767 ± 0.01	68.6 ± 0.15	9.6 (9.5 ± 0.10)

[a] Devices were fabricated with the conventional structure (ITO/PEDOT:PSS/BHJ layer/ETLs/Al). [b] The maximum value was obtained from the best performance among the fabricated devices; the average values were obtained from 10 devices.

The calculated energy level of the pristine BHJ was −5.63 eV; then, the shifted properties appeared upon the introduction of ETLs. The calculated energy level of the active layer introducing **PFN** was −5.28 eV, while in the case of **ANT** it was −5.38 eV. In addition, the introduction of hybrid ETLs resulted in the calculated energy level = −5.38 eV, which was identical to the case of the **ANT** (as shown in Fig. 4a and c). The calculated work function (E_f) of the pristine Al electrode was −4.79 eV; then, the shifted properties appeared upon the introduction of ETLs, and likewise for the BHJ. The introduction of **PFN**, **ANT**, and hybrid ETLs resulted in respective energy level properties of −5.43 eV, −5.40 eV, and −5.41 eV (as shown in Fig. 4b and c).

A diagram of the energy level between the BHJ layer and Al electrode after the introduction of ETLs is presented in Fig. 4d. In contrast to the large barrier of 0.84 eV at the interface between the BHJ and Al, the interfaces of BHJ/**PFN**/Al exhibited a small barrier of 0.15 eV. Furthermore, the smallest barrier of about 0.02–0.03 eV appeared at the interfaces of films introducing **ANT** and hybrid ETLs; then the internal electric field favorable for carrier transport properties was formed. As a result, V_{OC} increased further than for the pristine BHJ by the introduction of all ETLs; in particular, J_{SC} and FF greatly increased resulting in higher PCE upon the introduction of **ANT** and hybrid ETLs. These results suggest that the **ANT** has an alignment which matches better with the acceptor, $PC_{71}BM$

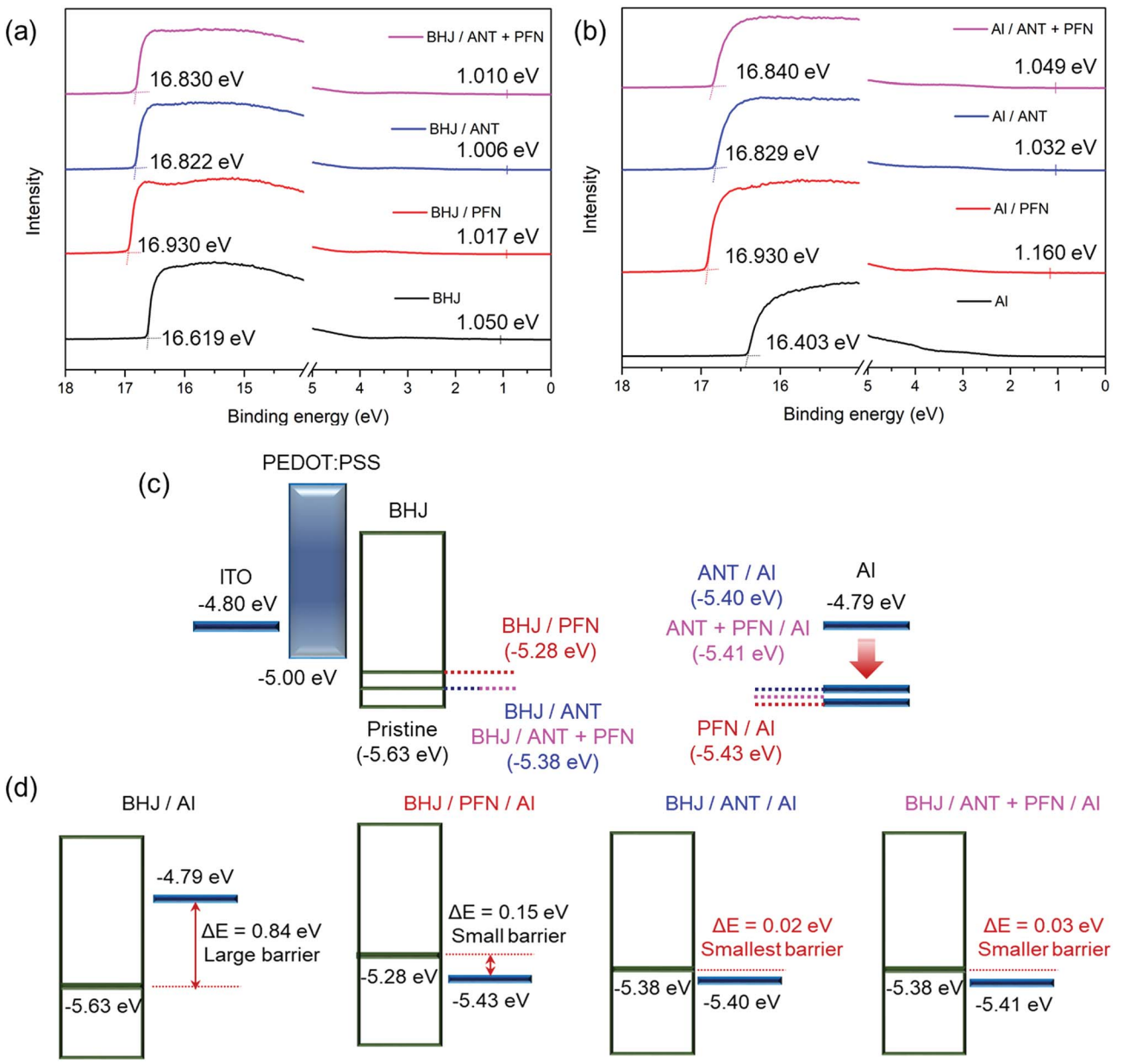

Fig. 4 UPS characteristics of the (a) BHJ/ETLs and (b) ETLs/Al electrode and schematic energy level diagram of (c) entire devices, and (d) between BHJ and ETLs.

($E_{LUMO} = -4.20$ eV), rather than **PFN** ($E_{HOMO} = -5.57$ eV, $E_{LUMO} = -2.68$ eV), as shown in Fig. S4 (ESI†).[52,57]

In Fig. S8 (ESI†), the *J–V* characteristics measured under various incident light conditions of 10–100 mW cm^{-2} are presented. In addition, the properties of carrier transport and collection were identified through analyzing normalized photocurrent characteristics (shown in Fig. S9, ESI†) based on Fig. S8 (ESI†). The *J–V* characteristics and normalized photocurrent characteristics measured under various conditions of light intensity can provide insight into the carrier recombination.[58,59]

The *J–V* variation corresponding to the various intensities of incident light was observed in all of the films. In particular, the behavior of recombination can be inferred based on the analysis of normalized photocurrent characteristics.[58] The monomolecular (trap-assisted) recombination was identified through the photocurrent characteristics of the reverse bias range from approximately 0.6 V, and the position of maximum power point (MPP), at which the saturation begins toward the reverse bias range. Furthermore, the bimolecular recombination was identified through the photocurrent characteristics of the forward bias range from MPP. Consequently, the films of pristine BHJ and BHJ/**PFN** exhibited a broad spread of photocurrent properties indicating high carrier recombination. However, suppressed recombination properties were observed from the narrow photocurrent properties in films with BHJ/**ANT** and BHJ/hybrid ETLs, respectively. They were attributed to the favorable carrier transport properties resulting from the introduction of **ANT** and hybrid ETLs.

For a deeper study into the recombination tendency, the characteristics of J_{SC} and V_{OC}–light intensity dependence were analyzed (shown in Fig. S9e and f, respectively, ESI†). In general, the J_{SC} shows a power-law relationship $J_{SC} \propto I^{\alpha}$ with light intensity (I) and exhibits suppressed bimolecular recombination characteristics as the slope (α) approximates a value of $\alpha = 1$.[13,14,58,59] The introduction of **ANT** and hybrid ELTs resulted in $\alpha = 0.986$ and 0.991, respectively, indicating a linear dependence with suppressed bimolecular recombination characteristics. Furthermore, the V_{OC} shows a relationship of $V_{OC} \propto kT/q \ln(I)$ with light intensity (where k is the Boltzmann constant, T is the absolute temperature, and q denotes the elementary charge). It then shows suppressed monomolecular recombination characteristics when the slope approximates kT/q.[15,16,58] The introduction of **ANT** and hybrid ETLs resulted in a slope of $1.029kT/q$ and exhibited suppressed monomolecular recombination characteristics. These results suggest that the introduction of **ANT** and hybrid ETLs can control the carrier recombination more effectively than the **PFN** (the slopes of $\alpha = 1.125$ and $1.030kT/q$). Consequently, the introduction of **ANT** and hybrid ETLs resulted in the minimization of the energy barrier at the interface between the BHJ and Al, and effectively controlled the carrier recombination by the formation of favorable energy level alignment for carrier transport. This effect enabled the great enhancement of V_{OC}, J_{SC}, and FF.

As shown in Fig. 5, the changes to the surface and internal structure of the BHJ film resulting from the introduction of ETLs were analyzed with the atomic signals detected through XPS analysis.[60–62] The respective films were fabricated under conditions identical to those used for fabricating devices 1–4. The introduction of ETLs resulted in the greatest changes in C1s signals, F1s signals, and N1s signals of the surface of the BHJ film. The film incorporated with **PFN** exhibited surface characteristics almost similar to those of the pristine BHJ film, with decreased C1s signals and F1s signals (shown in Fig. 5a–c). By contrast, the films that were incorporated with either **ANT** or hybrid ETLs formed N1s signals (at 398–402 eV) while F_{1s} signals (at 686–690 eV) disappeared (shown in Fig. 5c and d). The reduction in F1s signals corresponding to organic fluoride (at 688–689 eV) and formation of N1s signals corresponding to the substituted amine functional group (*e.g.* azanetriyl group) (C–N(C)–C, at 400.3 eV), suggest that the coverage of the BHJ film became excellent due to the **ANT** and hybrid ETLs.[62,63] In particular, a shift of N1s signals (approximately 0.1 eV) was observed in the hybrid ETLs. This is due to the partial polarization occurring at the C–N chain through the interaction between the high electron deficient diethanolamine group of **ANT** and the high electron rich amino group of **PFN**, as predicted by the results of ESP analysis (shown in Fig. 1).[64] Furthermore, by these interactions, the relative resonance occurred at the C–N chain resulting in a shift of N_{1s} signals.[65] Accordingly, the carrier transport pathway increased in hybrid ETLs resulting in an effective reduction in carrier recombination.

As shown in Fig. S10 (ESI†), the atomic signals of the films with the respective incorporated ETLs were detected through XPS depth-profiling analysis.[66] The sputtering process was carried out at a rate of 4 nm min^{-1} (the thickness of the BHJ layer was approximately 100 nm) under repetitive scanning. The surface of the film (at sputter time = 0 min) incorporated with **PFN** exhibited a higher level of F1s signals, while N1s signals were hardly observed. As the sputtering time increased (toward the bottom of the BHJ layer), F1s signals decreased and N1s signals increased. By contrast, the film incorporated with either **ANT** or hybrid ETLs exhibited a higher level of N1s signals on its surface with the absence of F1s signals. Subsequently, as the sputtering time increased, the F1s signals initially increased, and then decreased. Detailed comparisons between N1s signals and F1s signals are presented in Fig. 5e and f. Such changes in atomic signals suggest that BHJ films with **PFN** and **ANT** ETLs had different configurations. As a result, the introduction of **PFN** generated partial interfacial mixing on the surface of the BHJ layer, resulting in the exposure of PTB7-Th (by the increase of F1s signals). By contrast, the introduction of **ANT** and hybrid ETLs led to uniform coverage properties of the BHJ layer, resulting in formulation of a structure capable of playing the role of ETLs without interfacial mixing.

The interfacial mixing created by the introduction of **PFN** was identified through FE-SEM and AFM analyses. As shown in Fig. 6, respective ETLs were introduced on the pristine BHJ, and the resulting surface and cross-sectional properties were analyzed. The BHJ film with **PFN** exhibited a rough morphology ($R_q = 1.680$ nm) and cross-sectional images showed large agglomerates while the pristine BHJ film showed a less rough morphology ($R_q = 1.545$ nm) (Fig. 6a–f). By contrast, the

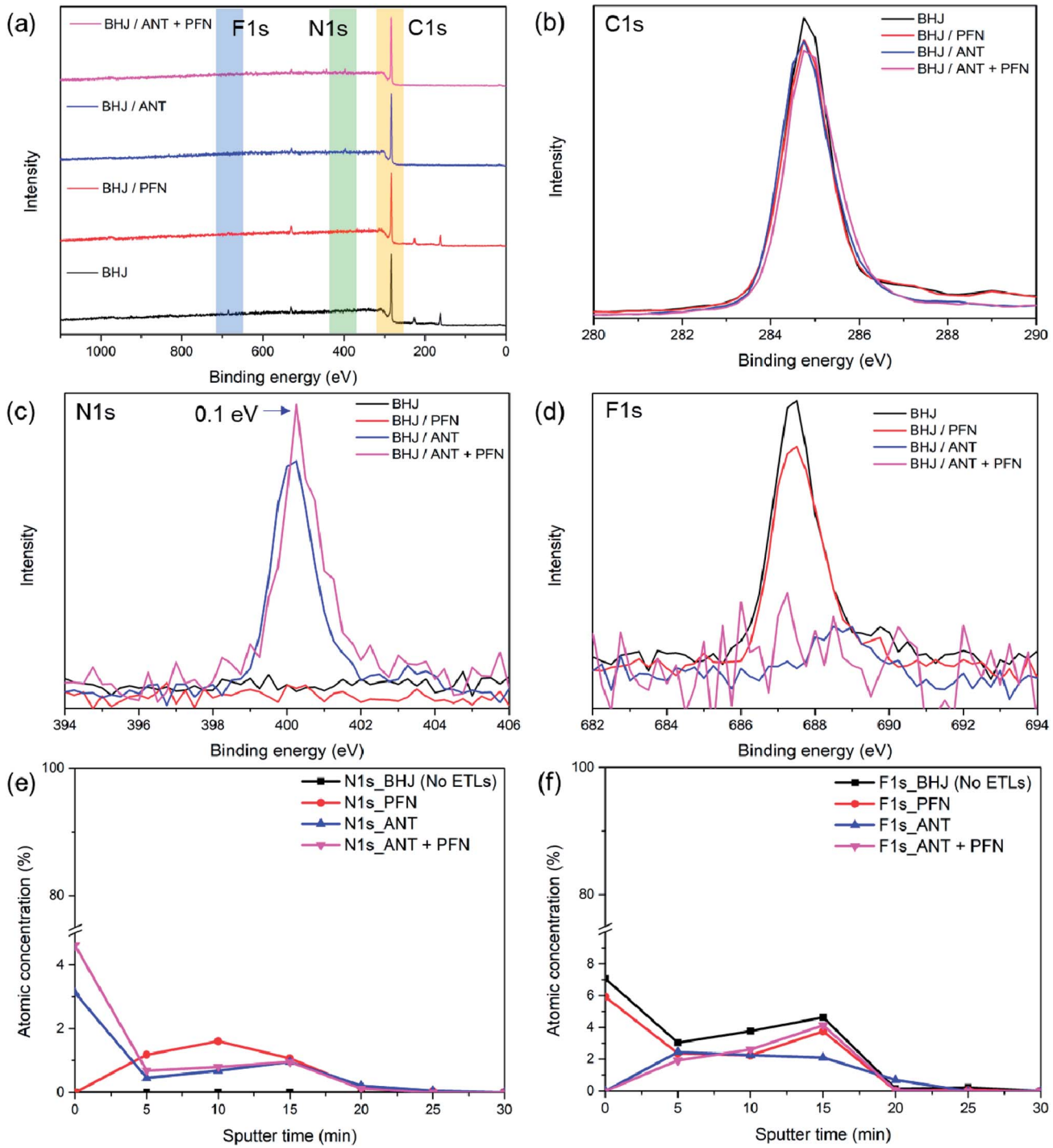

Fig. 5 Surface XPS characteristics of pristine BHJ, BHJ/**PFN**, BHJ/**ANT**, and BHJ/**ANT** + **PFN** films with respect to (a) surface analysis, (b) C1s atomic signals, (c) N1s atomic signals, (d) F1s atomic signals, and XPS depth profiling characteristics of (e) N1s atomic signals and (f) F1s atomic signals.

introduction of **ANT** exhibited a clean morphology (R_q = 1.531 nm) and cross-sectional images with comparatively smaller agglomerates resulting from well-matched interfacial properties between the ETLs and BHJ layer (Fig. 6g–i). Furthermore, the introduction of hybrid ETLs resulted in a relatively rough morphology (R_q = 1.633 nm), while it formed nanostructured phase separation. The cross-sectional images of the film with hybrid ETLs appeared to be clean, similar to those for **ANT**. Due to these well-matched interfacial properties and nanostructured phase separation of **ANT** and hybrid ELTs, the carrier transport was enhanced and carrier recombination was suppressed. Consequently, the introduction of **PFN** resulted in an increase in

V_{OC} due to the decreased energy barrier between the BHJ layer and Al electrode; however, the increase in J_{SC} and FF significantly lagged behind that of **ANT** due to large agglomerates through interfacial mixing. By contrast, the introduction of **ANT** and hybrid ETLs brought about suppressed carrier recombination properties by the synergistic effects of a relatively small energy barrier and uniform morphology that exhibited higher PCE resulting from increases in V_{OC}, J_{SC}, and FF.

In Fig. S11 (ESI†), the GIWAXS characteristics and line-cut characteristics of BHJ films with incorporated ETLs are presented. Fig. S11a–d (ESI†) show the 2D characteristics of the crystalline structure of BHJ films, while Fig. S11e (ESI†) illustrates the out-of-plane and in-plane patterns. The pristine BHJ film exhibited a strong (010) peak due to π–π stacking at $q_z = 1.42$ Å^{-1} ($d_{\pi-\pi} = 0.44$ nm) and a peak due to lamellar stacking at $q_{xy} = 0.28$ Å^{-1} ($d_{\text{lamellar}} = 2.24$ nm), resulting from the formation of a face-on dominant crystalline structure (Fig. S11a, ESI†). Furthermore, the ring-like peak, created by the randomly oriented ordering of $PC_{71}BM$, appeared at $q_z = 1.39$ Å^{-1} ($d_{\pi-\pi} = 0.45$ nm).[67,68] The BHJ film with **PFN** exhibited a relatively weak (010) peak at $q_z = 1.43$ Å^{-1} with a slightly reduced $d_{\pi-\pi}$ spacing distance ($d_{\pi-\pi} = 0.44$ nm). This weak peak intensity suggested a relatively low π–π stacked molecular order (Fig. S11b, ESI†). By contrast, the film with **ANT** and hybrid ETLs exhibited

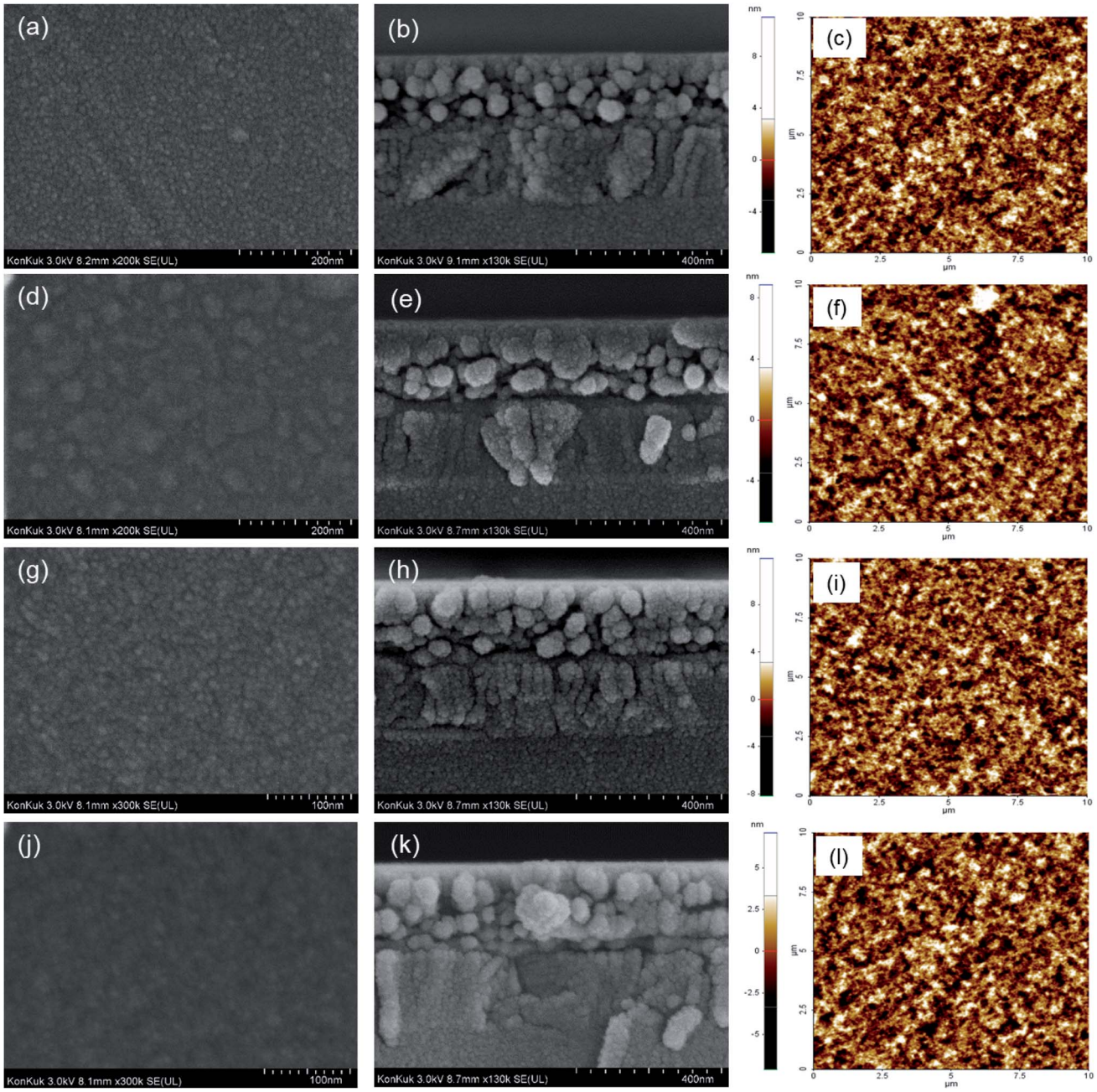

Fig. 6 FE-SEM top view (left section), cross-sectional view (middle section) and AFM morphology characteristics of (a–c) BHJ, (d–f) BHJ/**PFN**, (g–i) BHJ/**ANT**, and (j–l) BHJ/**ANT** + **PFN** films.

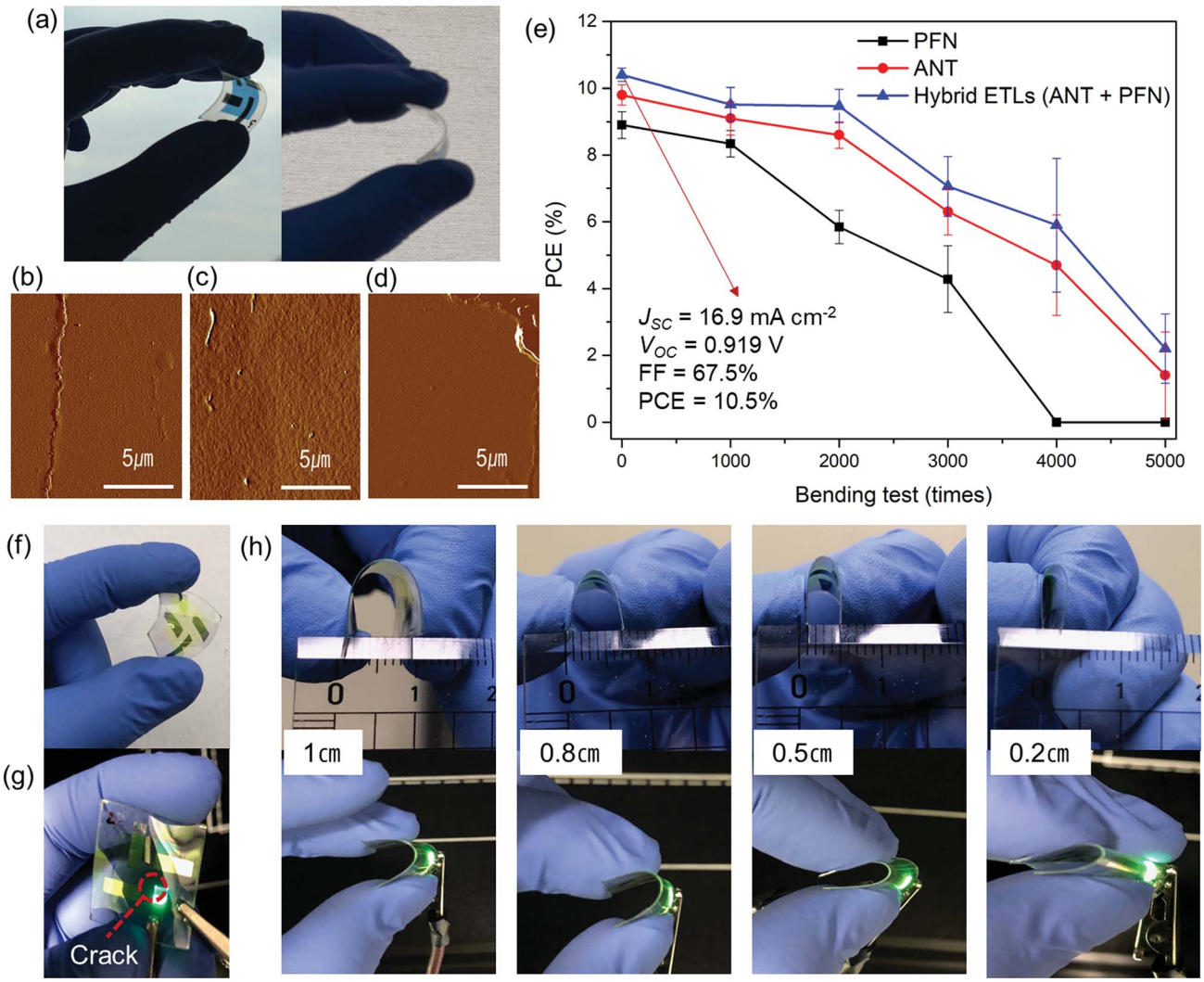

Fig. 7 (a) Images of the fabricated flexible OSCs on PEN substrate based on the non-fullerene BHJ layer, and AFM images of the surface of (b) the **PFN** incorporated device and (c) **ANT** incorporated device, (d) hybrid ETL incorporated device after mechanical bending test (5000 times), and (e) trend of performances of flexible OSCs fabricated with **PFN** and hybrid ETLs, (f) image of the fabricated flexible OLEDs based on green polymers incorporated with hybrid ETLs, (g) luminescence characteristics of the flexible device with cracks after the mechanical bending test, and (h) luminescence characteristics with respect to bending radii of 1 cm, 0.8 cm, 0.5 cm, and 0.2 cm.

a strong (010) peak at $q_z = 1.56$ Å^{-1} ($d_{\pi-\pi} = 0.49$ nm). This high peak intensity suggested higher π–π stacked molecular order in the BHJ film with **ANT** and hybrid ETLs (Fig. S11c and d, ESI†). Consequently, the **ANT** and hybrid ETLs enabled the formation of a uniform morphology without interfacial mixing and higher π–π stacked molecular order. The formation of a highly π–π ordered molecular structure and uniform morphology favorable for carrier transport resulted in high performance.

The introduction of ETLs was helpful for the suppression of carrier recombination properties; therefore, the carrier transport properties were improved. We analyzed the electron and hole mobility characteristics in order to identify the carrier transport properties (Fig. S12 and Table S2, ESI†). The electron and hole mobility characteristics were calculated through the Mott–Gurney space charge limited current (SCLC) formula with the fabrication of the electron-only device (ITO/ZnO/BHJ layer/ETLs/Al) and hole-only device (ITO/PEDOT:PSS/BHJ layer/MoO_3/Ag).[69,70]

$$J = \frac{9}{8}\mu\varepsilon_0\varepsilon_r V^2 \Big/ L^3 \quad (2)$$

where μ is the charge carrier mobility, ε_0 is the free-space permittivity, ε_r is the dielectric constant of the semiconductor, V is the applied voltage, and L is the thickness of the semiconductor layer.

As shown in Table S2 (ESI†), the pristine BHJ exhibited μ_e (electron mobility) = 5.02×10^{-4} cm^2 V^{-1} s^{-1}, and μ_h (hole mobility) = 3.11×10^{-4} cm^2 V^{-1} s^{-1}, while the BHJ film with **PFN** exhibited $\mu_e = 5.73 \times 10^{-4}$ cm^2 V^{-1} s^{-1} and $\mu_h = 3.27 \times 10^{-4}$ cm^2 V^{-1} s^{-1}. The resultant respective ratios of μ_e/μ_h of 1.61 and 1.75 suggested an imbalance in carrier mobility properties. By contrast, the BHJ film with **ANT** exhibited $\mu_e = 1.91 \times 10^{-3}$ cm^2 V^{-1} s^{-1} and $\mu_h = 2.05 \times 10^{-3}$ cm^2 V^{-1} s^{-1}, while the BHJ

film with hybrid ETLs exhibited $\mu_e = 2.12 \times 10^{-3}$ cm^2 V^{-1} s^{-1} and $\mu_h = 2.01 \times 10^{-3}$ cm^2 V^{-1} s^{-1}. The resultant respective ratios of μ_e/μ_h of 0.93 and 1.05 suggested balanced carrier recombination properties. The introduction of **ANT** and hybrid ETLs exhibited suppressed carrier recombination properties, resulting in greatly enhanced carrier transport properties.

In the present study, the excellent properties of **ANT** and hybrid ETLs were analyzed from the following three perspectives. First, **ANT** and hybrid ETLs minimized energy loss through the formation of the smallest energy barrier between the BHJ layer and Al electrode. Second, **ANT** and hybrid ETLs exhibited suppressed carrier recombination properties by showing linear dependence among V_{OC}, J_{SC}, and light intensity under the conditions of varied light irradiation. Third, the suppressed carrier recombination properties were manifested through a uniform morphology by introduction of **ANT** and hybrid ETLs. Consequently, the carrier transport properties were increased with enhanced internal electric field, resulting in enhanced V_{OC}, J_{SC}, and FF. Furthermore, the performances of the devices fabricated with ETLs at various thicknesses are presented in Tables S3–S5 (ESI†). **PFN** exhibited the best performance at 10 nm, while **ANT** and hybrid ETLs showed relatively thickness-independent properties with respect to thickness. This tendency is a result of the excellent electronic properties of **ANT** and hybrid ETLs.

We also fabricated devices based on a non-fullerene system (PBDB-T:ITIC-M) with novel ETLs (as shown in Fig. S13 and Table S6, ESI†). The performances of devices increased greatly with ETLs similar to the fullerene system. Device 7 with **ANT** exhibited a PCE of 11.2% ($J_{SC} = 17.8$ mA cm^{-2}, $V_{OC} = 0.919$ V, and FF = 68.7%) and device 8 with hybrid ETLs exhibited a PCE of 11.4% ($J_{SC} = 18.1$ mA cm^{-2}, $V_{OC} = 0.919$ V, and FF = 68.3%). The performance enhancement was attributable to the synergistic effects of energy level matching and uniform morphology. Furthermore, the stability of devices based on fullerene and non-fullerene systems is shown in Fig. S14 and S15 (ESI†). Both of these systems showed decreased PCE due to a reduction of J_{SC} and FF, and the devices (devices 4 and 8) with hybrid ETLs exhibited the most excellent stability. The enhancement in performance and stability can be attributed to advancements in OSCs by application to the non-fullerene system as well as to the fullerene system.

We have also developed OLEDs with novel ETLs for the application of enhanced carrier transport properties. OLEDs based on the green polymer as an emitting layer were fabricated with a conventional structure (ITO/PEDOT:PSS/photoactive layer/ETLs/Al) identical to OSCs. The optoelectronic performances and CIE 1931 chromaticity diagrams are presented in Fig. S16 and Table S7 (ESI†). Device 9 without ETLs exhibited a maximum luminescence of 943 cd m^{-2}. By contrast, device 11 with **ANT** and device 12 with hybrid ETLs exhibited a maximum luminescence of 17 257 cd m^{-2} (current efficiency = 2.199 cd A^{-1}, power efficiency = 1.382 lm W^{-1}) and 17 057 cd m^{-2} (current efficiency = 2.544 cd A^{-1}, power efficiency = 1.598 lm W^{-1}), respectively. These performances exceed those realized by device 10 with **PFN**. Furthermore, the CIE 1931 chromaticity diagrams and coordinates are presented in Fig. S17 and Tables S8–S11 (ESI†). The devices introducing hybrid ETLs showed more pure green color with CIE 1931 coordinates ($x, y = 0.2936$, 0.5819) that are similar to pure green ($x, y = 0.3000$, 0.6000).

In Fig. 7a–e and Table 2, the performances of the fabricated flexible OSCs incorporated with **PFN**, **ANT**, and hybrid ETLs are exhibited. The flexible OSCs fabricated on the PEN substrate were subjected to 5000 mechanical bending tests at a constant

Table 2 Photovoltaic performances of the fabricated flexible OSCs (PBDB-T:ITIC-M) after 5000 mechanical bending tests[a]

ETLs and bending test	J_{SC} [mA cm^{-2}]	V_{OC} [V]	FF [%]	PCE[b] [%]
PFN (initial)	16.7 ± 0.31	0.889 ± 0.01	59.2 ± 0.17	9.1 (8.9 ± 0.20)
PFN (after 5000 times)	0.027 ± 0.00	0.010 ± 0.00	0 ± 0.00	0 (—)
ANT (initial)	16.8 ± 0.19	0.909 ± 0.01	63.6 ± 0.25	10.0 (9.8 ± 0.15)
ANT (after 5000 times)	9.8 ± 2.17	0.707 ± 0.01	19.4 ± 5.05	2.1 (1.4 ± 0.65)
Hybrid ETLs (initial)	16.8 ± 0.13	0.909 ± 0.01	67.3 ± 0.27	10.5 (10.4 ± 0.12)
Hybrid ETLs (after 5000 times)	11.2 ± 1.99	0.707 ± 0.01	27.4 ± 2.68	2.8 (2.2 ± 0.57)

[a] Flexible devices were fabricated with the conventional structure (ITO(PEN)/PEDOT:PSS/BHJ layer/ETLs/Al). [b] The maximum value was obtained from the best performance among the fabricated devices; the average values were obtained from 5 devices.

Table 3 Optoelectronic performances of the fabricated flexible OLEDs with respect to bending radius[a]

Bending radius [cm]	Turn-on voltage [V]	Current efficiency [cd A^{-1}]	Power efficiency [lm W^{-1}]	Luminescence [cd m^{-2}]
Initial (0)	3	3.6598	2.6832	14 289
1	3	3.7137	2.2933	12 708
0.8	3	3.4164	1.9454	11 004
0.5	3	2.6493	1.4786	10 997
0.2	3	1.6301	1.0404	9824

[a] Flexible devices were fabricated with the conventional structure (ITO(PEN)/PEDOT:PSS/BHJ layer/ETLs/Al).

speed and characterized every 1000 times. After 400 bending tests, the **PFN** device exhibited a PCE of 0% showing that it was electrically disabled with a largely cracked surface (Fig. 7b and e). In contrast, the **ANT** and hybrid ETL incorporated device exhibited higher mechanical strength with a less rough surface after 5000 bending tests (Fig. 7c–e). This higher mechanical strength resulting from well-matched interfacial properties could be helpful for flexible electronic applications (detailed data in Tables S12–S14, ESI†). In Fig. 7f–h and Table 3, operating images and performances of the fabricated flexible OLEDs introducing hybrid ETLs under various bending radius conditions are exhibited. When the device was bent to radii in the order of 1 cm, 0.8 cm, 0.5 cm, and 0.2 cm, the flexible OLEDs still exhibited a luminescence of 9824 cd m^{-2}, showing a reduction rate of 31.2% from the initial state. These results indicate that hybrid ETLs have high carrier transport and

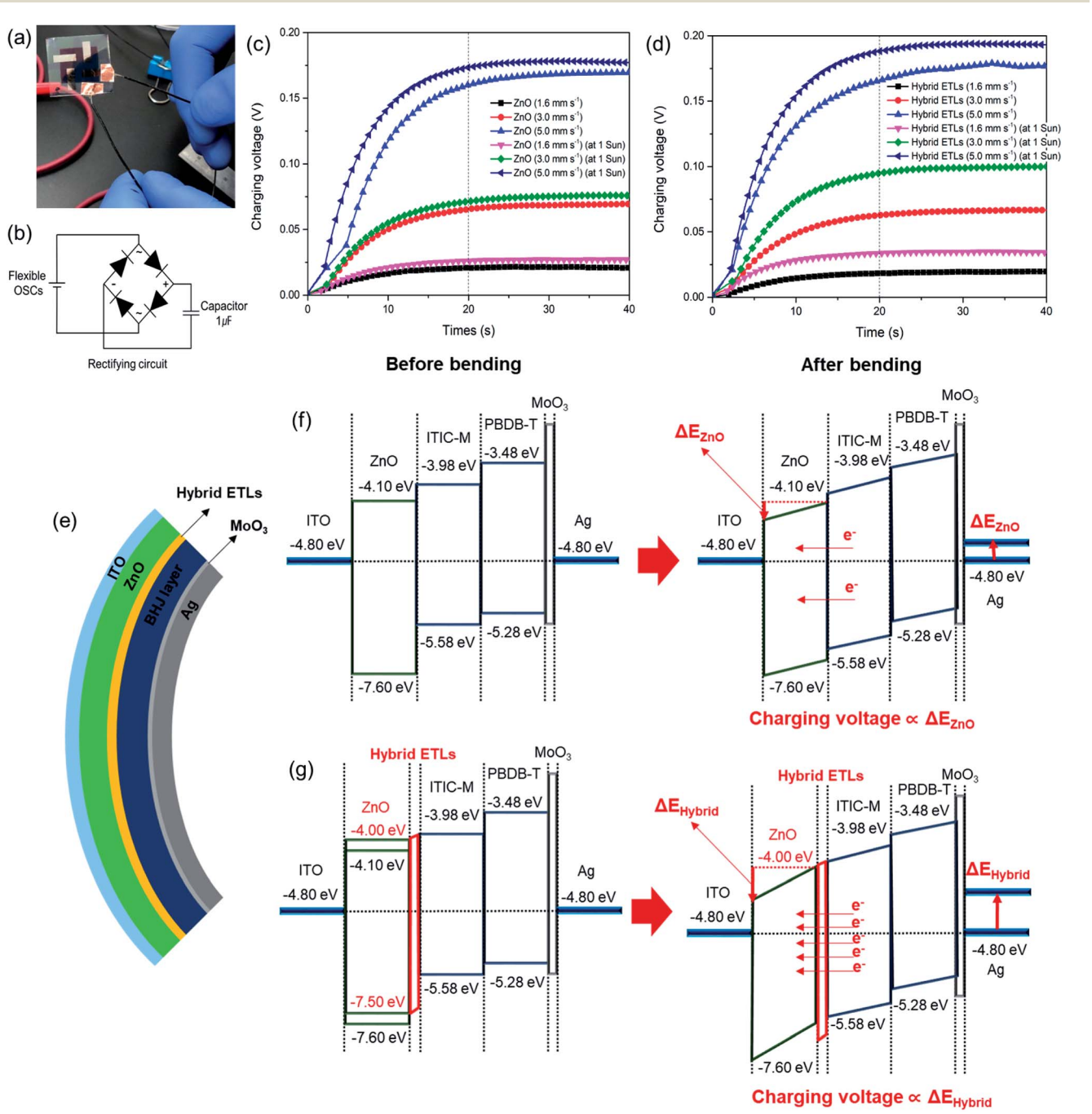

Fig. 8 (a) Image of flexible OSCs connected to a rectifying charge system, (b) schematic image of the rectifying circuit, and charging voltage–time characteristics of the (c) reference device (only pristine ZnO) and (d) hybrid ETL incorporated device with respect to deflection distance of mechanical bending (at a frequency of 1 Hz, in the dark or under 1 sun irradiation conditions). (e) Image of bent flexible OSCs and schematic images of energy level change (f) reference flexible OSCs (only ZnO) and (g) flexible OSCs incorporated with hybrid ETLs with respect to bending conditions in the rectifying charging circuit (under 1 sun irradiation conditions).

mechanical strength. Consequently, the hybrid ETLs can also be applied in the flexible electronics field. Based on these results, it is confirmed that the application of novel anthracene based ETLs showing excellent carrier transport properties was a good strategy for the fabrication of superior optoelectronic devices.

High carrier transport properties can be helpful in the field of organic nano-generators. We fabricated a flexible inverted structure (ITO/ZnO/BHJ layer/MoO_3/Ag) device introducing hybrid ETLs for demonstrating carrier transport – charging dependence (shown in Fig. 8). ZnO has been used for nano-generation because of its intrinsic piezoelectric potential from mechanical deformation.[71] Consequently, the inverted structured flexible OSCs incorporating ZnO and ETLs can be used to prepare a nano-generator.[72,73] We constituted a rectifying charging circuit connected with two types of flexible OSCs (incorporating either pristine ZnO or ZnO/hybrid ETLs, shown in Fig. 8a and b). The flexible OSCs were subjected to mechanical bending load at a rate of 1.6 mm s^{-1}, 3.0 mm s^{-1}, and 5.0 mm s^{-1}. In this rectifying circuit, the generated charges from the bended flexible OSCs accumulated in the capacitor ($C = 1$ μF), exhibiting time-dependent charging performance. The charging voltage performance was initially increased, then saturated after 20 s. The charging voltage performances of the reference device (pristine ZnO) reached 0.020 V, 0.066 V, and 0.159 V for the bending rate under dark conditions. Then, those of the reference device reached 0.026 V, 0.071 V, and 0.173 V with light irradiation under 1 sun conditions (shown in Fig. 8c) and exhibited enhancements of 30%, 7.57%, and 8.80%, respectively. By contrast, the charging voltage performance of the hybrid ETL incorporated device reached 0.018 V, 0.063 V, and 0.165 V under dark conditions. Then, that of the hybrid ETL incorporated device reached 0.034 V, 0.095 V, and 0.189 V under 1 sun conditions (shown in Fig. 8d) and exhibited large enhancements of 88.9%, 50.8%, and 14.5%, respectively. In addition, in Fig. 8e–g, the energy diagram changes of the bended flexible OSCs are exhibited. The reference device (shown in Fig. 8f) showed a smaller energy level shift (ΔE_{ZnO}) while the hybrid ETLs (shown in Fig. 8g) showed a higher energy level shift (ΔE_{Hybrid}) resulting in enhanced charging voltage because of high carrier transport properties.[71] Consequently, these results indicate that the high carrier transport of hybrid ETLs can be applied not only in the field of flexible organic optoelectronics but also in flexible ONGs.

Conclusions

We synthesized anthracene based derivatives exhibiting parallel dominant molecular stacking characteristics. Then, electronic devices (rigid type and flexible type) were fabricated with ETLs. **PFN**, that has been commercialized as an ETL, resulted in an increase of carrier recombination because of interfacial mixing. By contrast, **ANT** has parallel dominant stacking properties and partial polarization properties that can be caused high carrier transport properties. Thus, the hybridization of **ANT** with **PFN** can offer high carrier transport properties when they are introduced as ETLs. The hybrid ETLs exhibited suppressed carrier recombination properties through energy level matching, as well as a uniform morphology and face-on dominated molecular stacking, thus suggesting an enhancement of carrier transport. As a result, the V_{OC}, J_{SC}, and FF were improved and higher PCEs of 9.6% in the fullerene system and 11.4% in the non-fullerene system were exhibited. Furthermore, the flexible OSCs and OLEDs fabricated with hybrid ETLs exhibited high mechanical strength and performance resulting from carrier transport. In particular, the hybrid ETLs can be applied in the field of flexible ONGs exhibiting enhanced charging voltage under 1 sun irradiation conditions. These results suggest that **ANT** and hybrid ETLs are applicable in diverse fields of flexible OOEDs and ONGs contributing to the commercialization of organic optoelectronic devices.

Conflicts of interest

There are no conflicts to declare.

Acknowledgements

This research was supported by the New & Renewable Energy Core Technology Program of the Korea Institute of Energy Technology Evaluation and Planning (KETEP) grant funded by the Ministry of Trade, Industry & Energy (MI, Korea) (no. 20153010140030) and the Human Resources Program in Energy Technology of the Korea Institute of Energy Technology Evaluation and Planning (KETEP), granted financial resource from the Ministry of Trade, Industry & Energy, Republic of Korea (No. 20194010201790) and Korea Institute of Energy Technology Evaluation and Planning (KETEP) and the Ministry of Trade, Industry & Energy (MOTIE) of the Republic of Korea (No. 2018201010636A).

References

1 H. Fukagawa, T. Sasaki, T. Tsuzuki, Y. Nakajima, T. Takei, G. Motomura, M. Hasegawa, K. Morii and T. Shimizu, *Adv. Mater.*, 2018, **30**, 1–7.
2 H. Zhu, Y. Shen, Y. Li and J. Tang, *J. Semicond.*, 2018, **39**, 011011.
3 J. Zhao, Z. Chi, Z. Yang, X. Chen, M. S. Arnold, Y. Zhang, J. Xu, Z. Chi and M. P. Aldred, *Nanoscale*, 2018, **10**, 5764–5792.
4 H. Zhang, H. Yao, J. Hou, J. Zhu, J. Zhang, W. Li, R. Yu, B. Gao, S. Zhang and J. Hou, *Adv. Mater.*, 2018, 1800613.
5 W. Li, L. Ye, S. Li, H. Yao, H. Ade and J. Hou, *Adv. Mater.*, 2018, **30**, 1–8.
6 Z. Zheng, Q. Hu, S. Zhang, D. Zhang, J. Wang, S. Xie, R. Wang, Y. Qin, W. Li, L. Hong, N. Liang, F. Liu, Y. Zhang, Z. Wei, Z. Tang, T. P. Russell, J. Hou and H. Zhou, *Adv. Mater.*, 2018, 1801801.
7 Y. Zhang, B. Kan, Y. Sun, Y. Wang, R. Xia, X. Ke, Y. Q. Q. Yi, C. Li, H. L. Yip, X. Wan, Y. Cao and Y. Chen, *Adv. Mater.*, 2018, **30**, 1707508.

8 L. Meng, Y. Zhang, X. Wan, C. Li, X. Zhang, Y. Wang, X. Ke, Z. Xiao, L. Ding, R. Xia, H.-L. Yip, Y. Cao and Y. Chen, *Science*, 2018, **361**, 1094–1098.
9 Y. Im, S. Y. Byun, J. H. Kim, D. R. Lee, C. S. Oh, K. S. Yook and J. Y. Lee, *Adv. Funct. Mater.*, 2017, **27**, 1603007.
10 W. Zeng, H. Y. Lai, W. K. Lee, M. Jiao, Y. J. Shiu, C. Zhong, S. Gong, T. Zhou, G. Xie, M. Sarma, K. T. Wong, C. C. Wu and C. Yang, *Adv. Mater.*, 2018, **30**, 1704961.
11 G. Xie, J. Luo, M. Huang, T. Chen, K. Wu, S. Gong and C. Yang, *Adv. Mater.*, 2017, **29**, 1604223.
12 D. Di, L. Yang, J. M. Richter, L. Meraldi, R. M. Altamimi, A. Y. Alyamani, D. Credgington, K. P. Musselman, J. L. MacManus-Driscoll and R. H. Friend, *Adv. Mater.*, 2017, **29**, 1605987.
13 A. K. K. Kyaw, D. H. Wang, C. Luo, Y. Cao, T. Q. Nguyen, G. C. Bazan and A. J. Heeger, *Adv. Energy Mater.*, 2014, **4**, 1301469.
14 K. Cho, J. Kim, S. Y. Yoon, K. Y. Ryu, S. R. Jang, B. Lim and K. Kim, *Macromol. Rapid Commun.*, 2018, **39**, 1700630.
15 L. Zhang, B. Lin, B. Hu, X. Xu and W. Ma, *Adv. Mater.*, 2018, **30**, 1800343.
16 Q. An, J. Zhang, W. Gao, F. Qi, M. Zhang, X. Ma, C. Yang, L. Huo and F. Zhang, *Small*, 2018, 1802983.
17 M. Kuik, G. J. A. H. Wetzelaer, H. T. Nicolai, N. I. Craciun, D. M. De Leeuw and P. W. M. Blom, *Adv. Mater.*, 2014, **26**, 512.
18 M. Kuik, L. J. A. Koster, G. A. H. Wetzelaer and P. W. M. Blom, *Phys. Rev. Lett.*, 2011, **107**, 1–5.
19 M. Kuik, L. J. A. Koster, A. G. Dijkstra, G. A. H. Wetzelaer and P. W. M. Blom, *Org. Electron.*, 2012, **13**, 969.
20 C. Kasparek, I. Rörich, P. W. M. Blom and G. J. A. H. Wetzelaer, *J. Appl. Phys.*, 2018, **123**, 024504.
21 B. Kan, J. Zhang, F. Liu, X. Wan, C. Li, X. Ke, Y. Wang, H. Feng, Y. Zhang, G. Long, R. H. Friend, A. A. Bakulin and Y. Chen, *Adv. Mater.*, 2018, **30**, 1704904.
22 B. Xiao, J. Song, B. Guo, M. Zhang, W. Li, R. Zhou, J. Liu, H. B. Wang, M. Zhang, G. Luo, F. Liu and T. P. Russell, *J. Mater. Chem. A*, 2018, **6**, 957–962.
23 H. Xu, X. Fu, X. Cheng, L. Huang, D. Zhou, L. Chen and Y. Chen, *J. Mater. Chem. A*, 2017, **5**, 14689–14696.
24 E. J. Lee, M. H. Choi, Y. W. Han and D. K. Moon, *ACS Appl. Mater. Interfaces*, 2017, **9**, 44060–44069.
25 Q. Kang, L. Ye, B. Xu, C. An, S. J. Stuard, S. Zhang, H. Yao, H. Ade and J. Hou, *Joule*, 2018, 1–13.
26 W. Luo, C. Zeng, X. Du, C. Leng, W. Yao, H. Shi, X. Wei, C. Du and S. Lu, *J. Mater. Chem. C*, 2018, **6**, 4895–4902.
27 J. Xu, F. Peng, Y. Yang, L. Hu, R. He, W. Yang and Y. Cao, *Org. Electron.*, 2017, **49**, 1–8.
28 S.-J. Kwon, T.-H. Han, Y.-H. Kim, T. Ahmed, H.-K. Seo, H. Kim, D. J. Kim, W. Xu, B. H. Hong, J.-X. Zhu and T.-W. Lee, *ACS Appl. Mater. Interfaces*, 2018, **10**, 4874.
29 N. Wijeyasinghe, L. Tsetseris, A. Regoutz, W. Y. Sit, Z. Fei, T. Du, X. Wang, M. A. McLachlan, G. Vourlias, P. A. Patsalas, D. J. Payne, M. Heeney and T. D. Anthopoulos, *Adv. Funct. Mater.*, 2018, **28**, 1707319.
30 Q. Zhang, W. T. Wang, C. Y. Chi, T. Wächter, J. W. Chen, C. Y. Tsai, Y. C. Huang, M. Zharnikov, Y. Tai and D. J. Liaw, *Energy Environ. Sci.*, 2018, **11**, 682–691.
31 Q. Huang, S. Zhao, L. J. Guo, Z. Xu, P. Wang and Z. Qin, *Org. Electron.*, 2017, **49**, 123–128.
32 W. Zhang, W. Lan, M. H. Lee, J. Singh and F. Zhu, *Org. Electron.*, 2018, **52**, 1.
33 S. R. Hammond, J. Meyer, N. E. Widjonarko, P. F. Ndione, A. K. Sigdel, A. Garcia, A. Miedaner, M. T. Lloyd, A. Kahn, D. S. Ginley, J. J. Berry and D. C. Olson, *J. Mater. Chem.*, 2012, **22**, 3249–3254.
34 S. Nau, N. Schulte, S. Winkler, J. Frisch, A. Vollmer, N. Koch, S. Sax and E. J. W. List, *Adv. Mater.*, 2013, **25**, 4420.
35 C. Sun, Z. Wu, Z. Hu, J. Xiao, W. Zhao, H. W. Li, Q. Y. Li, S. W. Tsang, Y. X. Xu, K. Zhang, H. L. Yip, J. Hou, F. Huang and Y. Cao, *Energy Environ. Sci.*, 2017, **10**, 1784–1791.
36 R. Xu, K. Zhang, X. Liu, Y. Jin, X.-F. Jiang, Q.-H. Xu, F. Huang and Y. Cao, *ACS Appl. Mater. Interfaces*, 2018, **10**, 1939.
37 X. Gao, L. Yan, R. Xu and X. Sun, *J. Mater. Sci.: Mater. Electron.*, 2018, **29**, 19976–19984.
38 M. Gupta, D. Yan, J. Yao and C. Zhan, *ACS Appl. Mater. Interfaces*, 2018, **10**, 35896.
39 Z. Yu, B. Li and J. Ouyang, *Adv. Funct. Mater.*, 2018, **28**, 1802554.
40 Y. W. Han, J. Y. Choi, Y. J. Lee, E. J. Ko, M. H. Choi, I. S. Suh and D. K. Moon, *Adv. Mater. Interfaces*, 2018, 1801396.
41 J. Yang, Y. Lin, W. Zheng, A. Liu, W. Cai, X. Yu, F. Zhang, Q. Liang, H. Wu, D. Qin and L. Hou, *ACS Appl. Mater. Interfaces*, 2018, **10**, 22485.
42 J. Shi and C. W. Tang, *Appl. Phys. Lett.*, 2002, **80**, 3201–3203.
43 Y.-Y. Lyu, J. Kwak, O. Kwon, S.-H. Lee, D. Kim, C. Lee and K. Char, *Adv. Mater.*, 2008, **20**, 2720.
44 J. Huang, J. H. Su and H. Tian, *J. Mater. Chem.*, 2012, **22**, 10977–10989.
45 D. Liu, J. Li, J. Liu, X. Lu, M. Hu, Y. Li, Z. Shu, Z. Ni, S. Ding, L. Jiang, Y. Zhen, X. Zhang, H. Dong and W. Hu, *J. Mater. Chem. C*, 2018, **6**, 3856–3860.
46 T. Hinoue, Y. Shigenoi, M. Sugino, Y. Mizobe, I. Hisaki, M. Miyata and N. Tohnai, *Chem.–Eur. J.*, 2012, **18**, 4634.
47 N. Bouzayen, H. Sadki, M. Mbarek, M. Bouachrine, M. N. Bennani, J. Wery and K. Alimi, *Polym. Test.*, 2018, **66**, 78.
48 Y. Li, H. Meng, Y. Li, B. Pang, G. Luo and J. Huang, *New J. Chem.*, 2018, **42**, 18961–18968.
49 J. Mai, H. Lu, T. K. Lau, S. H. Peng, C. S. Hsu, W. Hua, N. Zhao, X. Xiao and X. Lu, *J. Mater. Chem. A*, 2017, **5**, 11739–11745.
50 C. Wang, Y. Luo, J. Zheng, L. Liu, Z. Xie, F. Huang, B. Yang and Y. Ma, *ACS Appl. Mater. Interfaces*, 2018, **10**, 10270.
51 D. J. Herman, J. E. Goldberger, S. Chao, D. T. Martin and S. I. Stupp, *ACS Nano*, 2010, **5**, 565–573.
52 H. J. Song, E. J. Lee, D. H. Kim, T. H. Lee, M. Goh, S. Lee and D. K. Moon, *Dyes Pigm.*, 2015, **113**, 210–218.
53 C. Lu, H.-C. Chen, W.-T. Chuang, Y.-H. Hsu, W.-C. Chen and P.-T. Chou, *Chem. Mater.*, 2015, **27**, 6837.

54 Q. Zhang, B. Kan, F. Liu, G. Long, X. Wan, X. Chen, Y. Zuo, W. Ni, H. Zhang, M. Li, Z. Hu, F. Huang, Y. Cao, Z. Liang, M. Zhang, T. P. Russell and Y. Chen, *Nat. Photonics*, 2014, **9**, 35–41.
55 S. Wen, W. Chen, G. Huang, W. Shen, H. Liu, L. Duan, J. Zhang and R. Yang, *J. Mater. Chem. C*, 2018, **6**, 1753–1758.
56 M. Gupta, D. Yan, J. Yao and C. Zhan, *Mater. Chem. Front.*, 2018, **2**, 1876–1883.
57 S. Nam, J. Seo, S. Woo, W. H. Kim, H. Kim, D. D. C. Bradley and Y. Kim, *Nat. Commun.*, 2015, **6**, 1–9.
58 A. K. K. Kyaw, D. H. Wang, V. Gupta, W. L. Leong, L. Ke, G. C. Bazan and A. J. Heeger, *ACS Nano*, 2013, **7**, 4569.
59 S. R. Cowan, A. Roy and A. J. Heeger, *Phys. Rev. B: Condens. Matter Mater. Phys.*, 2010, **82**, 245207.
60 H.-L. Hsu, Y.-C. Chao, Y.-H. Liao, C.-L. Chung, Y.-J. Peng, C.-P. Chen and R.-J. Jeng, *ACS Appl. Mater. Interfaces*, 2018, **10**, 8885.
61 C. Wang, C. Li, R. C. I. MacKenzie, S. Wen, Y. Liu, P. Ma, G. Wang, W. Tian and S. Ruan, *J. Mater. Chem. A*, 2018, **6**, 17662–17670.
62 A. Mohtasebi, T. Chowdhury, L. H. H. Hsu, M. C. Biesinger and P. Kruse, *J. Phys. Chem. C*, 2016, **120**, 29248.
63 B. Yu, X. Wang, X. Qian, W. Xing, H. Yang, L. Ma, Y. Lin, S. Jiang, L. Song, Y. Hu and S. Lo, *RSC Adv.*, 2014, **4**, 31782–31794.
64 P. C. Goh, K. Yao and Z. Chen, *J. Phys. Chem. C*, 2012, **116**, 15550.
65 I. Shimoyama, G. Wu, T. Sekiguchi and Y. Baba, *Phys. Rev. B: Condens. Matter Mater. Phys.*, 2000, **62**, 6053–6056.
66 L. Huang, G. Wang, W. Zhou, B. Fu, X. Cheng, L. Zhang, Z. Yuan, S. Xiong, L. Zhang, Y. Xie, A. Zhang, Y. Zhang, W. Ma, W. Li, Y. Zhou, E. Reichmanis and Y. Chen, *ACS Nano*, 2018, **12**, 4440–4452.
67 X. Xu, K. Fukuda, A. Karki, S. Park, H. Kimura, H. Jinno, N. Watanabe, S. Yamamoto, S. Shimomura, D. Kitazawa, T. Yokota, S. Umezu, T.-Q. Nguyen and T. Someya, *Proc. Natl. Acad. Sci. U. S. A.*, 2018, **115**, 4589.
68 Q. Wan, G. Xia, Z. Wang, W. Li, B. Guo, W. Ma, M. Zhang and Y. Li, *Adv. Funct. Mater.*, 2016, **26**, 6635.
69 Y. Zheng, G. Wang, D. Huang, J. Kong, T. Goh, W. Huang, J. Yu and A. D. Taylor, *Sol. RRL*, 2018, 1700144.
70 X. Yi, B. Gautam, I. Constantinou, Y. Cheng, Z. Peng, E. Klump, X. Ba, C. H. Y. Ho, C. Dong, S. R. Marder, J. R. Reynolds, S.-W. Tsang, H. Ade and F. So, *Adv. Funct. Mater.*, 2018, **28**, 1802702.
71 K. Y. Lee, B. Kumar, J. S. Seo, K. H. Kim, J. I. Sohn, S. N. Cha, D. Choi, Z. L. Wang and S. W. Kim, *Nano Lett.*, 2012, **12**, 1959–1964.
72 S. Y. Chung, S. Kim, J.-H. Lee, K. Kim, S.-W. Kim, C.-Y. Kang, S.-J. Yoon and Y. S. Kim, *Adv. Mater.*, 2012, **24**, 6022–6027.
73 G. C. Yoon, K.-S. Shin, M. K. Gupta, K. Y. Lee, J.-H. Lee, Z. L. Wang and S.-W. Kim, *Nano Energy*, 2015, **12**, 547–555.